Journal of Power Sources 196 (2011) 1818–1825

Contents lists available at ScienceDirect

Journal of Power Sources

journal homepage: www.elsevier.com/locate/jpowsour

# Investigation of degradation behavior of membrane electrode assembly with polytetrafluoroethylene/Nafion composite membrane

Ting-Chu Jao [a,b], Guo-Bin Jung [a,b,*], Pei-Hung Chi [c], Shih-Tsung Ke [d], Shih-Hung Chan [a,b]

[a] Department of Mechanical Engineering, Yuan Ze University, Taoyuan 320, Taiwan
[b] Fuel Cell Center, Yuan Ze University, Taoyuan 320, Taiwan
[c] Chung-Shan Institute of Science & Technology, Kaohsiung 840, Taiwan
[d] Department of Mechanical Engineering, Lee-Ming Institute of Technology, Taipei 243, Taiwan

ARTICLE INFO

*Article history:*
Received 6 September 2010
Accepted 20 September 2010
Available online 5 November 2010

*Keywords:*
Fuel cell
Composite membrane
Open circuit voltage degradation
Relative humidity cycling
Load cycling

ABSTRACT

The main purpose of this study is to investigate the accelerated degradation of the PTFE/Nafion membrane electrode assembly through open circuit voltage and relative humidity cycling. The state of a PTFE/Nafion membrane electrode assembly is evaluated in a fuel cell by monitoring the polarization curve, AC impedance, cyclic voltammetry, and linear sweep voltammetry data over time. The experimental results are then fitted to equations of an equivalent circuit. The results of the first 160 experimental cycles show that catalyst degradation is the main cause for the decay of the membrane electrode assembly. During the 160–520th cycles, the membrane electrode assembly experiences creep deformation, which is due to relative humidity cycling. During the 640–840th cycles, the degradation causes a gradual transition from minor to major membrane cracking; after which the combustion reaction dramatically accelerates membrane electrode assembly degradation.



## 1. Introduction

Due to their high efficiency, very low greenhouse gas emissions, and quiet and continuous operation mode, proton exchange membrane fuel cells (PEMFCs) are a promising power source. However, the high cost of the membrane electrode assembly (MEA) is the main reason why the commercialization of PEMFCs has been delayed.

The perfluorosulfonic acid proton exchange membrane is one of the key components of the MEA that has a significant effect on the overall cost and performance of a PEMFC. Many studies have attempted to develop low-cost composite membranes that can be prepared by impregnating a low-cost submicron porous support material, such as a polytetrafluoroethylene (PTFE) membrane, with a Nafion solution instead of using Nafion as a proton-conducting separator [1–9].

Due to the great mechanical strength of PTFE, inserting a porous PTFE film into a Nafion membrane reduces membrane thickness (the thickness of composite membranes prepared in our lab is about 15–25 μm and can be roughly controlled by fabrication conditions; the thicknesses of Nafion-211, Nafion-212, and Nafion-117 membranes are about 25, 50, and 175 μm, respectively). The lower thickness of PTFE/Nafion (PN) composite membranes allows them to have a lower proton resistance. Thus, PN composite membranes may have better performance in PEMFCs. Some studies have reported that PN composite membranes had similar PEMFC performances to those of DuPont Nafion-112 and better PEMFC performance than those of Nafion-115 and Nafion-117 [3–7]. The advantages of PN composite membranes are not only their low cost and thickness but also their good mechanical strength in both swollen and un-swollen states, good thermo-stability, and low dimension change ratio.

Tang et al. demonstrated that a PN composite membrane can be kept in a stable condition for more than 5000 cycles, about 40% higher than the pure Nafion membrane (about 3500 cycles) [10]. Several factors can affect the durability of PEMFCs [11–16]. Tang et al. did not test the durability of PN MEA operation in fuel cell discharge mode; therefore, catalyst layer degradation was not a concern. Electrocatalysts play an important role in improving the durability and lowering the cost of PEMFCs [13]. Many studies have shown that non-recoverable deterioration of PEMFC performance is primarily attributed to the degradation of Pt-based catalysts and proton exchange membranes in MEAs [14–16].

In summary, durability and cost are key issues for the commercialization of PEMFCs. Normally, a steady-state lifetime test can be employed to assess the lifetime of a fuel cell. However, this method is impractical as a durability test because it is time-consuming and

* Corresponding author at: Department of Mechanical Engineering, Yuan Ze University, No.135, Yuandong Rd., Zhongli City, Taoyuan County 320, Taiwan.
Tel.: +886 3 4638800x2469; fax: +886 3 455 5574.
*E-mail address:* guobin@saturn.yzu.edu.tw (G.-B. Jung).

0378-7753/$ – see front matter © 2010 Elsevier B.V. All rights reserved.
doi:10.1016/j.jpowsour.2010.09.068

costly. This study uses an accelerated degradation technique to show the durability of a PN membrane electrode assembly.

## 2. Experiment

### 2.1. Preparation of PTEE/Nafion membrane electrode assembly and cell specifications

Porous PTFE membranes with a thickness of $18 \pm 3$ μm, pore size of $0.5 \pm 0.1$ μm, and a porosity of $52 \pm 5\%$ were used as a supporting material of the composite membranes. A Nafion solution of 5 wt% of 1100EW Nafion diluted in a mixture of water, isopropyl alcohol, methanol, and unspecified ethers [17] was used. The procedure for the preparation of PN composite membranes has been described in a previous paper [8].

The catalyst HiSPEC 4310 (39.6 wt% Pt/C, Johnson Matthey) and 5 wt% 1100EW Nafion solution (DuPont Co.) were mixed and dispersed in isopropyl alcohol by ultrasonication for 30 min to form a uniform catalyst ink. The ratio of Pt/C loading to solid Nafion was maintained at 2:1. The MEA was fabricated using the catalyst-coated membrane (CCM) method. The catalyst ink was applied onto the PN membrane with a spray gun. The carrier gas was air, and the pressure was about 15–20 psi. Air was supplied by an air pump equipped with water, oil, and particle filters. The Pt catalyst loading was 0.5 mg $cm^{-2}$ on both the anode and cathode. The CCM was sandwiched by a gas diffusion layer (SGL, 10BC) without a hot press.

In this study, a homemade cell was used. The homemade cell had three components; these were an insulating plate, a collecting plate, and a flow field plate, which were made of glass fiber, gold-coated brass, and graphite, respectively. The channel depth, channel width, and rib width of the serpentine flow field plate were 1 mm each. The reaction area was 25 $cm^2$.

### 2.2. Experimental procedures, parameters, and apparatus

The operating conditions of the activation process were a cell temperature of 65 °C, a hydrogen flow rate of 500 sccm and an air flow rate of 1250 sccm, both at relative humidity (RH) 100%. The discharge voltage was maintained at 0.4 V for 30 min. Performance tests were carried out to ensure that the specimen was successfully activated. The criterion of stability was defined as follows. The change rate of current density at 0.6 V, as defined in Eq. (1), was measured and recorded. The activation process was considered to be complete when the change rate of any two consecutive events was within ±5%. Once the specimen condition was stable, the operation temperature was raised to 80 °C gradually to accelerate the degradation process.

$$\text{Change rate} = \frac{i_{0.6\,\text{V},n} - i_{0.6\,\text{V},n-1}}{i_{0.6\,\text{V},n-1}} \times 100\% \quad (1)$$

The three steps of an accelerated degradation cycle are:

Step 1: maintain open circuit voltage (OCV) at RH 100%;
Step 2: discharge at 0.6 V at RH 100%;
Step 3: discharge at 0.6 V at RH 0% (bypass).

Step 1 represents the aging mode at high temperature and humidity, Step 2 is the discharge aging mode at high temperature and humidity, and Step 3 represents the discharge aging mode at high temperature and low humidity. The MEA was subjected to various aging processes during each complete degradation cycle. For example, the aging process for voltage cycling occurred between Steps 1 and 2 and the aging process for humidity cycling from Steps 2 to 3, whereas from Steps 3 to 1, potential cycling, humidity cycling, and OCV at high temperature and low humidity occurred.

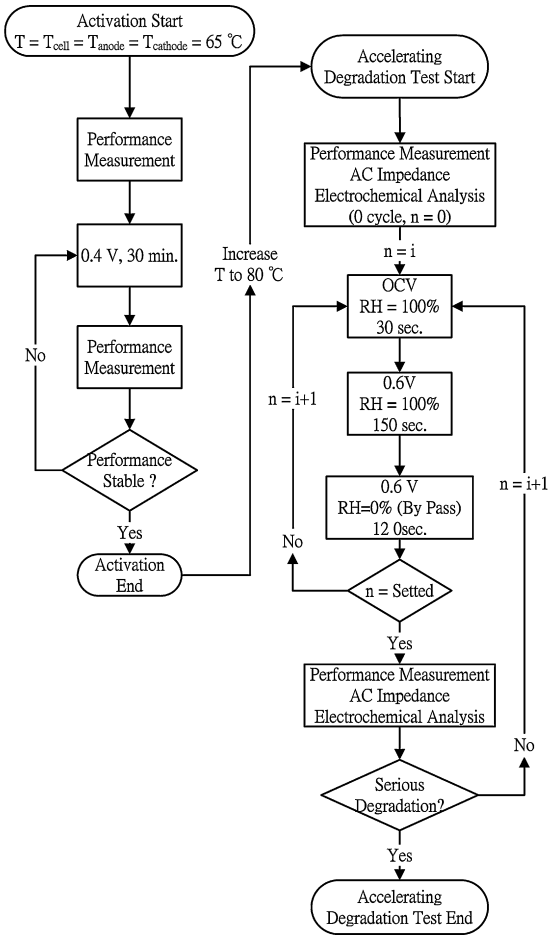


**Fig. 1.** Experimental flowchart.

Accordingly, these processes caused the membrane, ionomer, catalyst, and carbon support to age. During the degradation cycle, the hydrogen flow rate was maintained at 251 sccm at the anode, and the air flow rate was 997 sccm at the cathode. The total time for a complete cycle was 5 min. Fig. 1 shows the detailed procedure and the time of operation.

Specimen performance was characterized by a constant voltage scanning method, which began from OCV to 0.3 V. The scanning rate of change was 0.025 V $step^{-1}$, the velocity rate of change was 30 s $step^{-1}$, and the recording frequency was 3 s $point^{-1}$. Three scans were performed for each measurement. This study used the trimmean function to remove 20% of the extreme values and then retrieved the average of the resulting values.

The operating conditions of polarization measurement were 80 °C, RH 100%, 500 sccm hydrogen flow rate, and 1250 sccm air flow rate. No back pressure was used during the experiment. The operation conditions for AC impedance measurement were the same as those for polarization measurement. AC impedances were measured the current density loadings of 100, 200, and 500 mA $cm^{-2}$. The scanned frequency range was 10k–0.1 Hz, and the amplitude was 5% of the current loading. The measurements were repeated three times for each load condition.

The following operating conditions were used for the electrochemical analysis. The gas fed to the anode was 500 sccm of hydrogen humidified to RH 100%. The anode served as both the counter electrode and the reference electrode. Humidified nitrogen at RH 100% was supplied at the cathode (working electrode). The scanning speed of the cyclic voltammetry (CV) method was 50 mV $s^{-1}$, the sampling speed was 1 mV $point^{-1}$, and the scanning

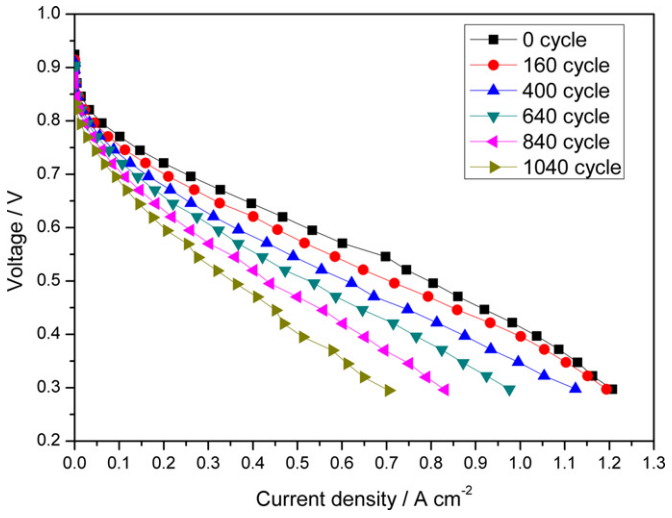


**Fig. 2.** Polarization curve during the accelerated degradation process.

range was approximately 0–0.8 V. The scanning range was adjusted after membrane breakage. The scanning speed of the linear sweep voltammetry (LSV) method was 1 mV $s^{-1}$, and the other operating conditions were the same as those of the CV method.

The supply gases in the activation, polarization tests, accelerated degradation process, AC impedance, and electrochemical analysis were provided by the same system, FC 5100 (CHINO Corporation, Japan), which also performed the measurements in each of these stages. The electrochemical analysis used CHI 1127A (CH Instruments, Inc., USA). The electrochemical surface area (ESA) in a CV measurement was calculated as follows [18]:

$$\mathrm{ESA} = \frac{100000 \times A_\mathrm{d}}{C \times m \times v} \tag{2}$$

$$A_\mathrm{d} = \int_{0.05}^{0.4} (i - i_\mathrm{DL})\mathrm{d}V \tag{3}$$

The ESA in Eq. (2) is measured in $m^2\ g^{-1}$, where $A_d$ is the integral area of the hydrogen absorption peak (units of AV), c is the coefficient of hydrogen absorbed by platinum (value of 0.21 mC $cm^{-2}$), m is the amount of platinum at the cathode (units of mg), and v is the scanning speed of the CV method (units of mV $s^{-1}$) [18]. The integral area for the hydrogen absorption peak is computed in Eq. (3), where $i$ represents the measured current, and $i_{DL}$ is the current caused by electrode double-layer charging. The range of integration was initially between 0.05 and 0.4 V and was adjusted after the membrane breakage.

In the aging analysis, the AC impedance was curve-fitted with ZView software, and the polarization curve was curve-fitted to the following equation [19]:

$$V = V_0 - b \cdot \log(i) - i \cdot R_\mathrm{ohm} \tag{4}$$

where $V_0$ is defined as:

$$V_0 = V_\mathrm{theor} + b \cdot \log(i_0) \tag{5}$$

## 3. Results and discussion

### 3.1. Analysis of the polarization curve and AC impedance

Fig. 2 shows the polarization curve both before and after the accelerated degradation process. The 0.6 V current density decreased about 64% from the beginning to the end of aging process (from 0.553 A $cm^{-2}$ to 0.207 W $cm^{-2}$). In Fig. 2, the slope of the ohmic polarization zone during the 160th cycle is roughly the same as that of the initial ohmic polarization zone at zero cycles. This indicates that the aging between the 0 and 160th cycles is mainly caused by the aggregation and the grain growth of catalytic particles. The phenomenon results in a smaller electrochemistry activation area or even a loss of catalyst activity. From 160th cycle to 640th cycle, the slope of the ohmic polarization zone was observed to be steeper than the initial condition.

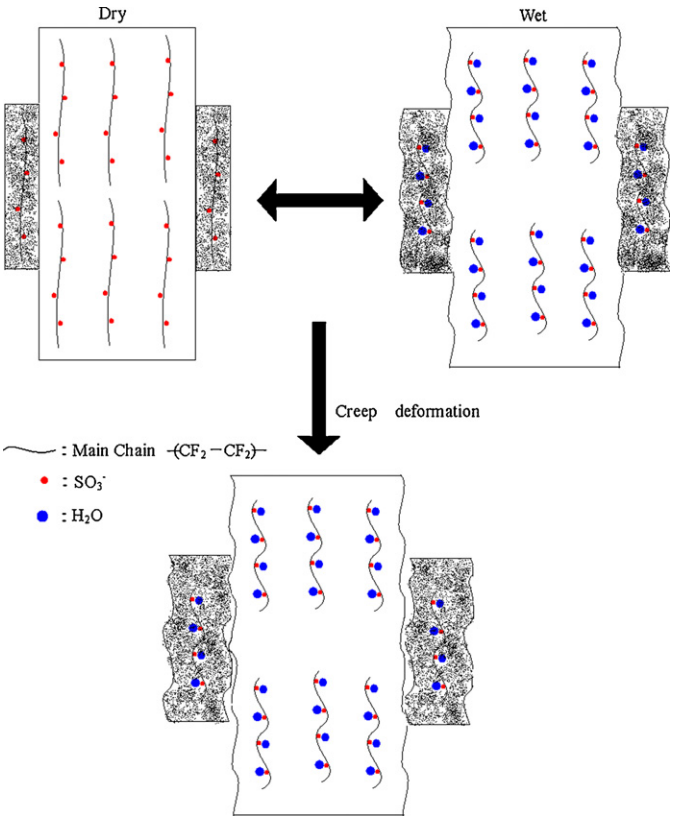


**Fig. 3.** A schematic of creep deformation.

The resistance of the ohmic polarization zone can be segregated into ion resistance, electron resistance, and interfacial contact resistance. The steeper slope of the aforementioned ohmic polarization zone indicates an increase of these resistances. The phenomenon of increasing ion resistance can result from a break of the side chain or the loss of a sulfonic acid group, both of which can occur on the catalyst layer or the membrane due to their high local temperatures. The increasing electron resistance results from carbon corrosion, whereas the increasing interfacial contact resistance results from creep deformation induced by the wet-and-dry cycle. Fig. 3 shows a schematic of the creep deformation. Creep deformation is the main reason that ohmic resistance rapidly increased after 640th cycle. Creep deformation is the special degradation mechanism of a non-homogeneous membrane, such as a PN membrane, in this study. A Nafion MEA should be free (or have minimal amounts) of creep deformation. Electrochemical analysis demonstrated that the transition zone from minor to major membrane breakage occurs between the 640th and 840th cycles. The 0.6 V current density of the decay rate of an accelerated degradation process was calculated by a linear regression analysis. The rates of 0.6 V current density decay were 0.391 mA $cm^{-2}$ $cycle^{-1}$ (before membrane breakage, 0–520th cycles) and 0.638 mA $cm^{-2}$ $cycle^{-1}$ (after membrane breakage, 880–1040th cycles). Membrane breakage has a crucial effect on MEA performance; therefore, the failure of fuel cells can be primarily attributed to membrane breakage. The most important consequences of membrane failure are safety issues, especially for stacks.

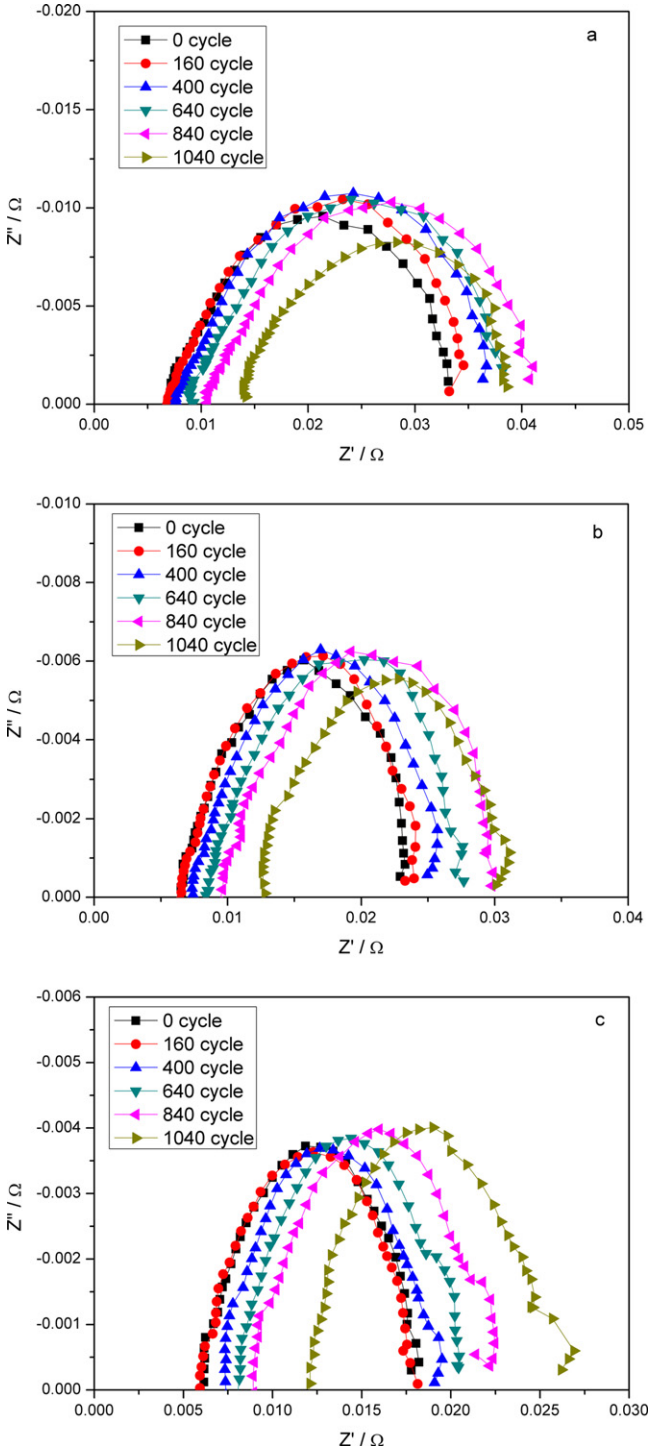


**Fig. 4.** AC impedance diagram during the accelerated degradation process under 100 mA cm$^{-2}$ (a), 200 mA cm$^{-2}$ (b), and 500 mA cm$^{-2}$ (c) discharge.

It is notable that the charge transfer semicircle of AC impedance depends upon the value of overpotential (i.e., the driving force), especially when the range of potential varies between different polarization zones [20].

The AC impedances of current density loadings of 100, 200, and 500 mA cm$^{-2}$ were analyzed and are shown in Fig. 4. The charge transfer semicircles all increased except during the 1040th cycles of Fig. 4(a) and (b), which indicates that the accelerated degradation process degrades the catalyst or ionomer.

The charge transfer semi circles, except the 1040th cycles of Fig. 4(a) and (b), are all in the activation polarization zone at 100 mA cm$^{-2}$ or 200 mA cm$^{-2}$. Compared to the other cycles, the 1040th cycles in Fig. 4(a) and (b) performance poorly, which led them to fall into the ohmic polarization zone, with reduced charge transfer resistance. All cycles in Fig. 4(c) belong to the ohmic polarization zone, and the high-frequency resistance increasing with the increasing cycle number implies that ohmic resistance increases with the aging process. There appeared to be no appreciable deviation of high-frequency resistance between the 160th cycle and the initial value demonstrated in Fig. 4. The 160th cycle charge transfer is slightly enlarged when the current density is 100 mA cm$^{-2}$. However, the resistance in the high-frequency range remains constant. This result conforms to the prediction of the polarization curve, where the catalyst aging mainly occurs before the 160th cycle, after which, creep deformation occurs. During creep deformation and before membrane breakage (160–640th cycles), ohmic slope (0.65–0.55 V) increased about 0.110 Ω cm$^2$, and high frequency resistance (1 kHz) increased about 0.058 Ω cm$^2$. The difference between the slope of the ohmic polarization zone and high frequency resistance is caused by the proton resistance of the catalyst layer; activation polarization may have slightly affected the slope of the ohmic polarization zone.

### 3.2. Analysis of electrochemistry

Fig. 5(a) and (b) shows the test results of CV and LSV, respectively. The peak voltage of hydrogen absorption decreases from 0.309 V (0 cycles) to 0.291 V (520 cycles) as the performance degrades, whereas the value of peak voltage increases after membrane breakage (880–1040th cycles). This deviates notably from the theoretical potential, which may result from the failure of the insulating effect between the anode and cathode gases after membrane breakage and thus from mixed potential at both sides. In Fig. 5(b), $i_{loss}$ is the sum of hydrogen crossover current and short-circuit current as defined in Eq. (6) [19]. The accelerated degradation process in every cycle of Fig. 5(b) eventually reaches a plateau at high voltage; therefore, no noticeable short-circuit condition is found in the MEA. The membrane itself is a poor electronic conductor; therefore, the $i_{loss}$ found in this study is concluded to be the hydrogen crossover

$$i_{loss} = i_{crossover} + i_{short} \quad (6)$$

Fig. 6(a) shows the correlation between ESA and $i_{loss}$. ESA was calculated from the CV test using Eq. (2). Fig. 6(a) indicates that ESA decreased from 40.514 m$^2$ g$_{pt}^{-1}$ (0 cycles) to 27.524 m$^2$ g$_{pt}^{-1}$ (520th cycle). The three boundary phase losses caused the ESA decrease, which resulted from the aging of the catalyst layer, including carbon corrosion and ionomer decomposition. Linear regression gives a decrease rate of 0.024 m$^2$ g$_{pt}^{-1}$ cycle$^{-1}$, and the decrease rate after membrane breakage (0.116 m$^2$ g$_{pt}^{-1}$ cycle$^{-1}$) is roughly five times greater than before membrane breakage. It is highly likely that membrane breakage (880–1040th cycles) encouraged the aging of the MEA by the combustion effect. This effect was caused by the mixture of hydrogen and air on the catalyst, which contributed to the higher rate of decrease. In reality, the value of the ESA approached zero when the experiment ended, and MEA performance was about 50% of its original value. Thus, we presume that CV is not applicable in this analysis after membrane breakage. In addition, the electrode double layer had nearly a 5% increase before membrane breakage, indicating that carbon corrosion contributed less to the aging of MEAs than did the other aging mechanisms before membrane breakage. Although the electrode double layer increase was larger after membrane breakage, its effect was still considered to be minor. Nevertheless, the electrode double layer

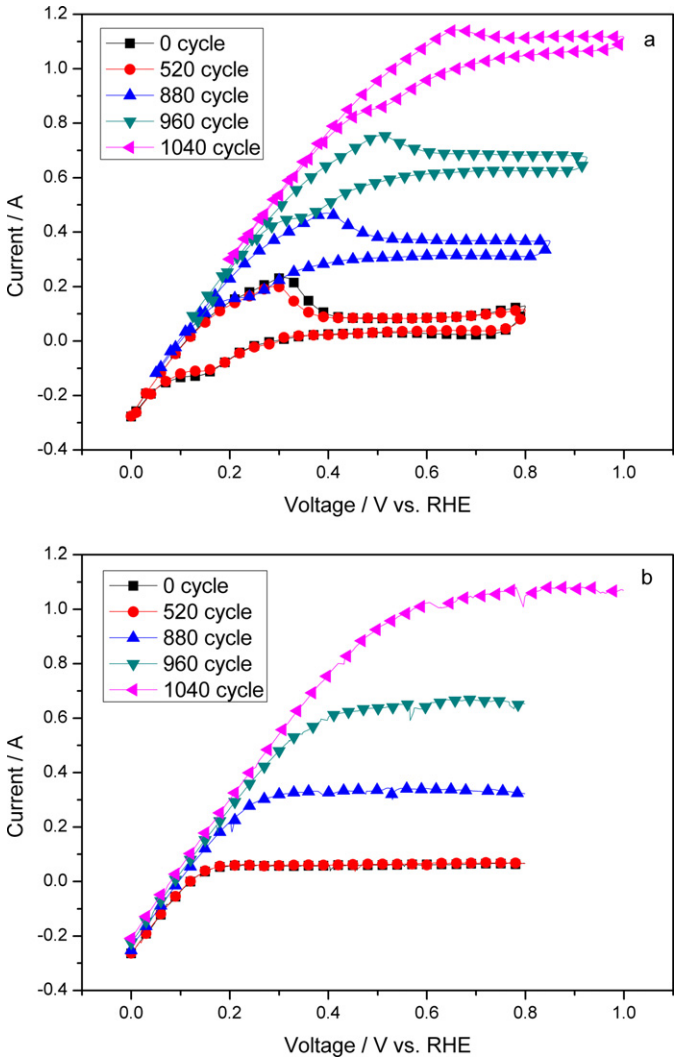


**Fig. 5.** CV (a) and LSV (b) diagram during the accelerated degradation process.

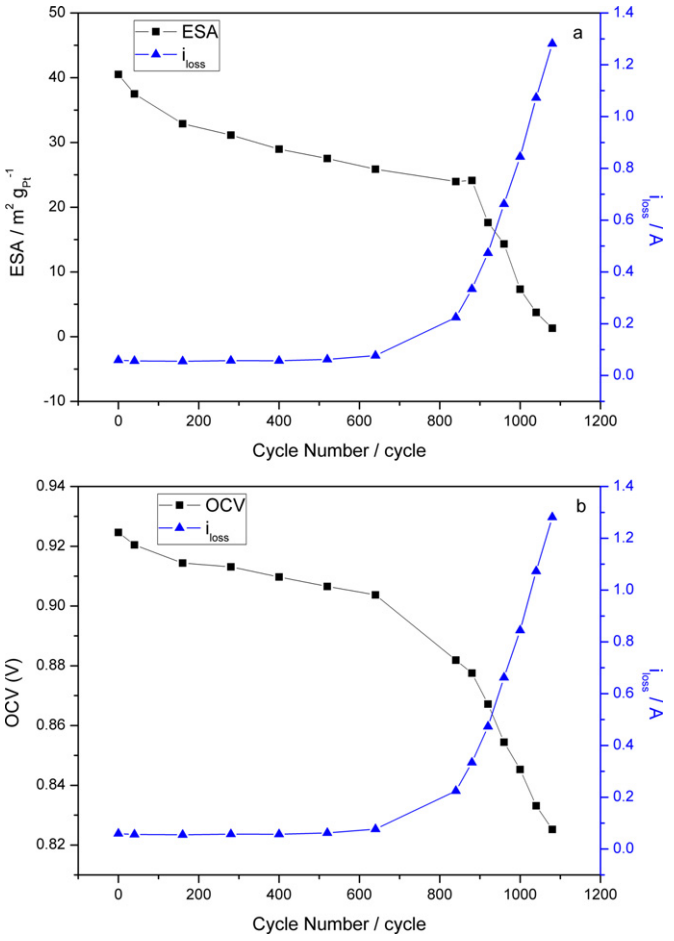


**Fig. 6.** ESA against $i_{loss}$ (a) and OCV against $i_{loss}$ (b) diagram during the accelerated degradation process.

increase may also be caused by mixing gases or mixed potential effects after membrane breakage. Therefore, we do not believe that carbon corrosion is a key factor throughout the process.

Fig. 6(b) represents the relationship between the OCV and $i_{loss}$. The OCV decreased from 0.925 V (0 cycles) to 0.907 V (520th cycle) before membrane breakage; this was caused by catalyst aging. Linear regression analysis gives the rate of decrease as 31 μV cycle$^{-1}$. After membrane breakage (880–1040th cycles), the aging of MEA was furthered by the increased possibility of a combustion reaction, causing the OCV to greatly decrease (a decrease rate of 226 μV cycle$^{-1}$, over eight times greater than before the membrane damage). There was a slight increase of $i_{loss}$ before membrane breakage (0–520th cycles) due to the membrane thinning effect by the hydroxyl produced from the side reaction and by $H_2O_2$. The $i_{loss}$ increase rate was 0.231 μA cm$^{-2}$ cycle$^{-1}$. The combustion after membrane breakage also remarkably raised the $i_{loss}$ increase rate to 191.937 μA cm$^{-2}$ cycle$^{-1}$, which is 830 times the value before membrane breakage.

### 3.3. Aging analysis

The experimental results of the accelerated degradation tests were curve-fitted using FCView and calculated by Eq. (4). The results of $V_0$, Tafel slope $b$, and internal resistance $R$ are plotted in Fig. 7(a–c), respectively. Fig. 7(a) shows that $V_0$ decayed with the accelerated aging process, but the rate of decay varied greatly before and after membrane breakage. Fig. 7(b) also demonstrates that $b$ increased with the aging process, which implies the degradation of the catalyst. The decrease of $V_0$ and the increase of $b$ correspond to the polarization curves. The major factor suggesting aging before 160 cycles is catalyst degradation, whereas the key factor of performance decay after 160 cycles is creep deformation. The study also showed that b decreased after membrane breakage, implying a significant increase of catalyst activity. A catalyst activity increase during the accelerated degradation test is not physically reasonable; therefore, the equation is not applicable after membrane breakage. The aforementioned $V_0$ is also a function of $b$; consequently, we must modify the fitted equation of $V_0$ after membrane breakage.

Fig. 7(c) shows the internal resistance $R$ increasing with the accelerated degradation process. Similarly, the increase rate of $R$ is notably larger after membrane breakage. The increase of $R$ is caused by a higher combustion reaction probability. The severe break of the side chain and loss of the sulfonic acid group were caused by the local high temperature in the combustion reaction. This explains the increase of $R$ after membrane breakage, whereas the $R$ increase can be attributed to lower ion conductivity, higher electron resistance, and higher interfacial contact resistance. As mentioned earlier, carbon corrosion is not significant to this accelerated degradation process. Ion conductivity was mainly changed by the break of the side chain and loss of the sulfonic acid group from the membrane and ionomer-on-catalyst layers, whereas interfacial contact resistance was caused by the creep deformation effect from the

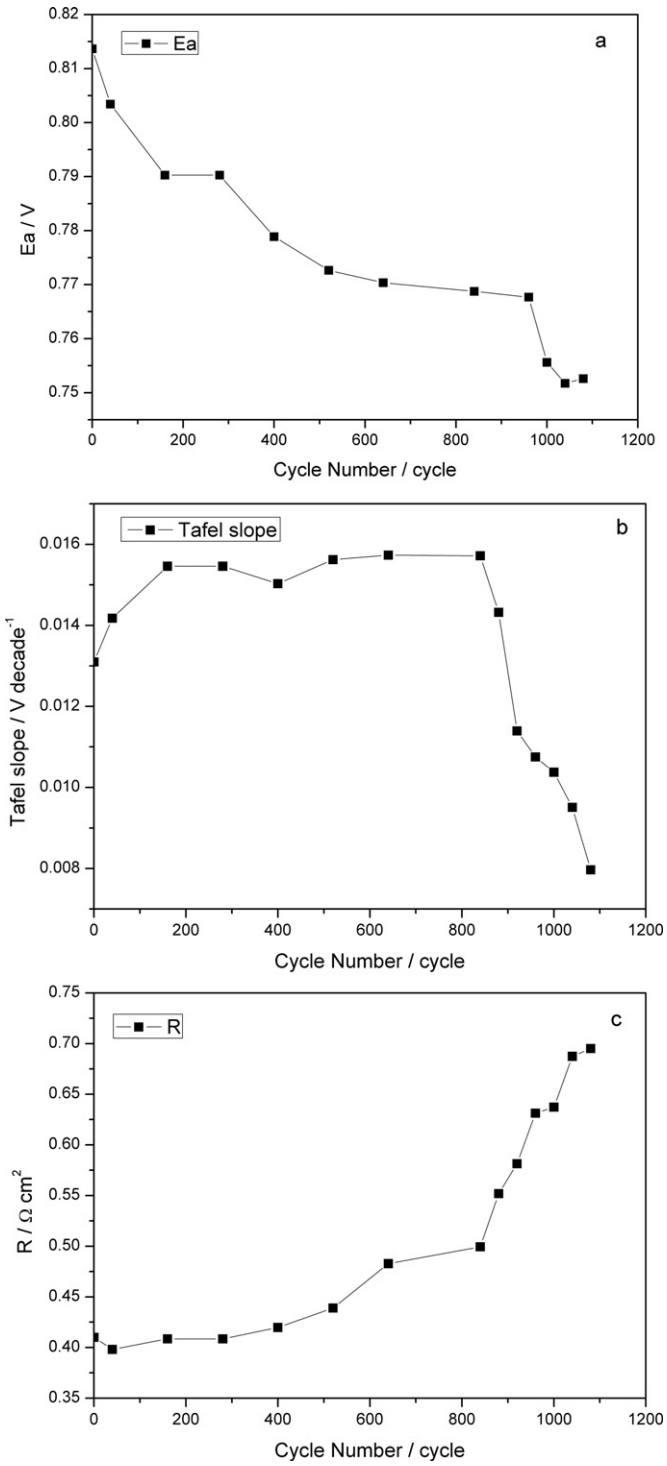


**Fig. 7.** $V_0$ (a), Tafel slope (b), and $R$ (c) change during the accelerated degradation process.

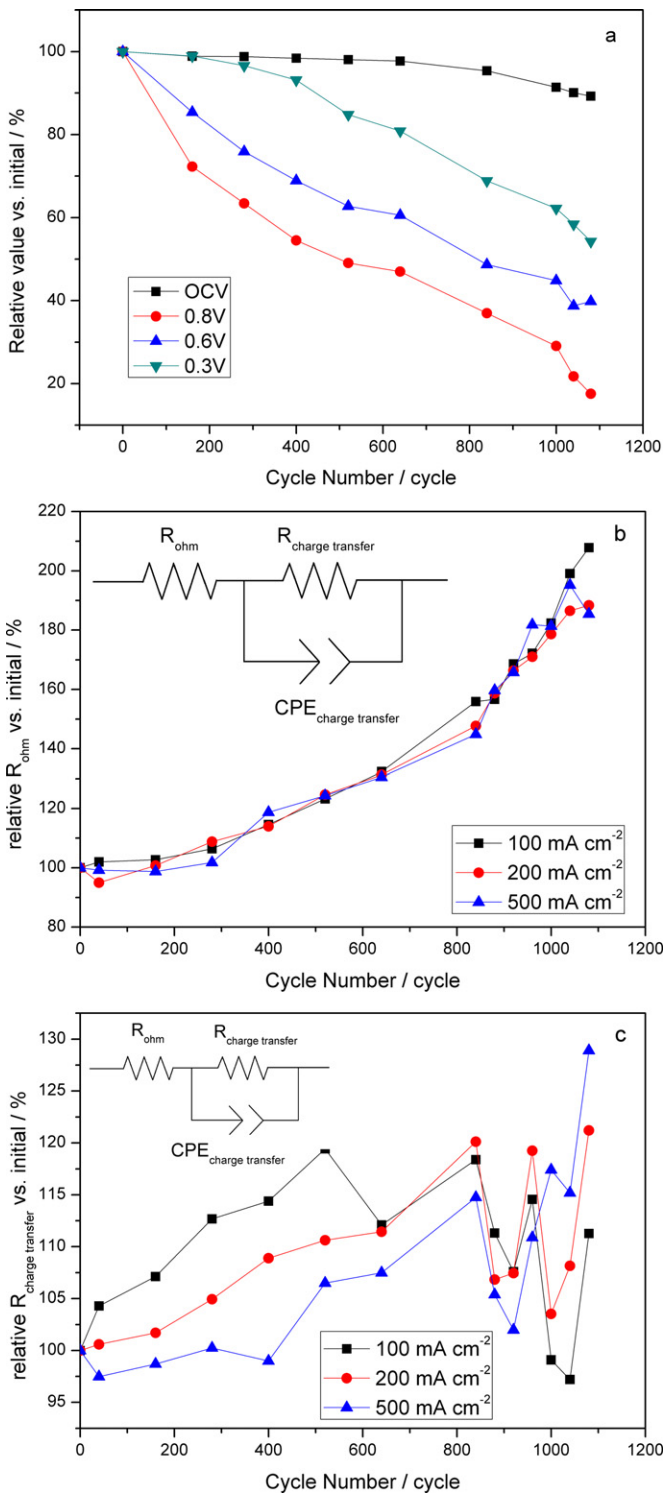


**Fig. 8.** Relative value of OCV and performance of different voltage (a), relative $R_{ohm}$ (b), and relative $R_{charge\ transfer}$ (c) during the accelerated degradation process.

dry–wet cycle. There was no obvious increase of $R$ prior to 160 cycles, which again confirms that catalyst degradation is a major cause of MEA aging before 160 cycles.

Fig. 8 shows the variation of OCV, performance, $R_{ohm}$, and $R_{charge\ transfer}$ with cycle number. As seen in Fig. 8(a), the OCV decreases by approximately 2% and 10% before and after membrane breakage. These results suggest that the degradation of the catalyst layer does not strongly influence OCV; thus, the membrane condition ($i_{loss}$) controls OCV. Fig. 8(a) shows that the decay magnitudes before and after the accelerated degradation process are very different under different operation voltages. These findings conform to the predictions of Eq. (7) and (8), which infer that the influence of $i_{loss}$ on the system is less under lower operating voltages [21].

$$V = V_0 - b \log\left(\frac{i + i_{loss}}{i_0}\right) - iR_i \quad (7)$$

$$V_0 = V_{theor} - b \log\left(\frac{i_{loss}}{i_0}\right) \quad (8)$$

**Table 1**
MEA aging conditions.

| Cycle | Relative $R_{ohm}$ at 500 mA cm$^{-2}$ (%) | Relative performance calculated by $R_{ohm}$ (%) | Relative ESA (%) | Relative performance at 0.6 V (%) | Relative Performance at 0.3 V (%) |
|---|---|---|---|---|---|
| 520 | 124.3 | 80.4 | 67.9 | 62.7 | 84.8 |
| 1080 | 185.4 | 53.9 | 9.3 | 39.8 | 54.2 |

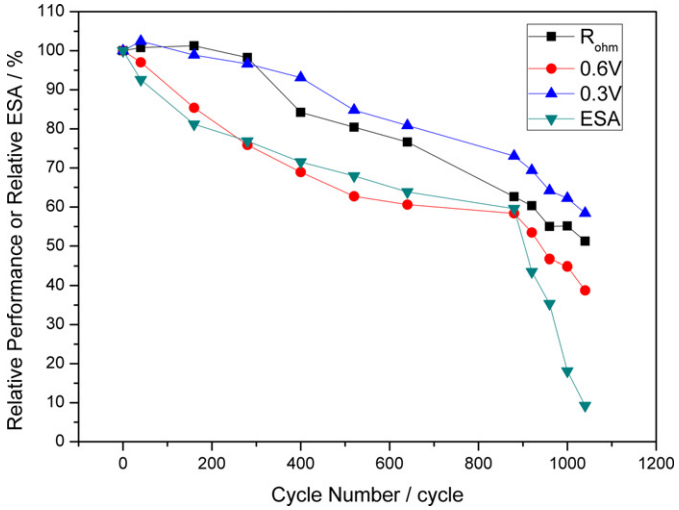


**Fig. 9.** Relative performance and relative ESA during the accelerated degradation process.

The above equations indicate a sudden drop of OCV due to an abrupt increase of $i_{loss}$. AC impedance is curve-fitted in the equivalent circuit in Fig. 8(b)–(c), and the corresponding $R_{ohm}$ and $R_{charge\ transfer}$ results are also shown. Before membrane breakage, $R_{ohm}$ and $R_{charge\ transfer}$ increased with accelerated degradation cycles, and the increase rate of $R_{ohm}$ accelerated after membrane breakage. The polarization curve and AC impedance analysis give the same prediction. The electrochemistry-related $R_{charge\ transfer}$ variability may contribute to the combustion reaction and mixed potential, which cause electrochemical reaction instability after membrane breakage. The relative $R_{ohm}$, ESA, and performance before membrane breakage and termination of the experiment are listed in Table 1. The relative performances at 0.6 V and 0.3 V before membrane breakage were 62.7% and 84.8%, respectively, whereas the relative ESA and calculated relative performance (with the use of $R_{ohm}$, $R_{ohm}^{-1}$) were 67.9% and 80.4%, respectively. The 0.6 V case shares a similar result with the ESA case because the 0.6 V case was more likely to be affected by the active polarization than was the case of ohmic polarization. However, the 0.3 V case was influenced more by the ohmic polarization than was the active polarization. The ESA inaccuracy caused by the mixed potential after membrane breakage also caused a mismatch between the relative performance of 0.6 V and relative ESA. However, the relative performance of 0.3 V still matched its relative $R_{ohm}$. The correlation between relative performances and relative ESA is illustrated in Fig. 9. Ultimately, we can make an estimation of the degree of MEA degradation by the change of $R_{ohm}$. Because the value of $R_{ohm}$ is close to the value of high-frequency impedance, the MEA condition can also be judged by the high-frequency resistance in this study.

## 4. Conclusion

We conclude that the major factor for MEA aging during this stage is catalyst degeneration based on its occurrence before the 160th cycle of the following: (i) the high frequency resistance of AC impedance was almost constant; (ii) the slope of the polarization curve in the ohmic polarization zone was unvaried; and (iii) the short-circuit current remained constant from the LSV result (only ESA decreased). Between the 160 and 520th cycles, LSV did not change, whereas ESA decreased. The slope of the ohmic polarization zone and the high-frequency resistance of AC impedance both indicated an increase of resistance. Thus, the major aging factor in this stage was ion conductivity loss, which could be due to creep deformation by the dry–wet cycle or the loss of the sulfonic acid group, with ESA as a secondary factor. The percentage of performance decay under 0.6 V is approximately the same as in the ESA case, whereas the decay under 0.3 V is roughly equal to that in the $R_{ohm}$ case. Subsequently, the membrane showed minor breakage and cracks, and complete membrane breakage occurred during the 880th cycle. An equation without $i_{loss}$ correction can no longer precisely describe the cell condition after membrane breakage. The mixed potential created serious errors of ESA, meaning that the ESA decay percentage cannot represent MEA degeneracy. However, the percentage increase of $R_{ohm}$ remains close to the performance decay under 0.3 V. A preliminary understanding of MEA can be obtained through the change of high-frequency resistance.

After membrane breakage, the combustion reaction remarkably increased the aging rate of performance. In conclusion, membrane breakage is the major factor causing the failure of MEA.

## Acknowledgement

The authors gratefully acknowledge the National Science Council of Taiwan under the contract NSC 98-2622-E-155 -074 -CC3 and NSC 98-3114-E-155 -001.

## References

[1] C. Liu, C.R. Martin, Journal of the Electrochemical Society 137 (1990) 510–515.
[2] B. Bahar, A.R. Hobson, J. Kolde, Ultra-thin film integral composite membrane, US Patent 5,547,551 (1996).
[3] K.M. Nouel, P.S. Fedkiw, Electrochimica Acta 43 (1998) 2381–2387.
[4] A.E. Steck, C. Stone, Substituted alpha, beta, beta-trifluorostyrene-based composite membranes, US Patent 5,834,523 (1998).
[5] F. Liu, B. Yi, D. Xing, J. Yu, H. Zhang, Journal of Membrane Science 212 (2003) 213–223.
[6] H.L. Lin, T.L. Yu, K.S. Shen, L.N. Huang, Journal of Membrane Science 237 (2004) 1–7.
[7] T.L. Yu, H.L. Lin, K.S. Shen, Y.C. Chang, G.B. Jung, J.C. Huang, Journal of Polymer Research 11 (2004) 217–224.
[8] H.L. Lin, T.L. Yu, L.N. Huang, L.C. Chen, K.S. Shen, G.B. Chung, Journal of Power Sources 150 (2005) 11–19.
[9] T.C. Jao, S.-T. Ke, P.H. Chi, G.B. Jung, S.H. Chan, International Journal of Hydrogen Energy 35 (2010) 6941–6949.
[10] H.L. Tang, M. Pan, F. Wang, Journal of Applied Polymer Science 109 (2008) 2671–2679.
[11] J. Yu, T. Matsuura, Y. Yoshikawa, M.N. Islam, M. Hori, Electrochemical and Solid State Letters 8 (2005) A156.
[12] J. Yu, T. Matsuura, Y. Yoshikawa, M.N. Islam, M. Hori, Physical Chemistry Chemical Physics 7 (2005) 373–378.
[13] Y. Shao, G. Yin, Y. Gao, Journal of Power Sources 171 (2007) 558–566.
[14] J. Xie, D.L. Wood, K.L. More, P. Atanassov, R.L. Borup, Journal of The Electrochemical Society 152 (2005) A1011–A1020.
[15] J.F. Wu, X.Z. Yuan, J.J. Martin, H.J. Wang, J.J. Zhang, J. Shena, Journal of Power Sources 184 (2008) 104–119.

[16] A. Collier, H.J. Wang, X.Z. Yuan, J.J. Zhang, D.P. Wilkinson, International Journal of Hydrogen Energy 31 (2006) 1838–1854.
[17] W.C.F. Grot, Nafion Perfluorinated Membranes Product Bulletin, DuPont Polymer Products Department, 1986.
[18] Y. Zhai, H. Zhang, D. Xing, Z. Shao, Journal of Power Sources 164 (2007) 126–133.
[19] K.R. Cooper, V. Ramani, J. M. Fenton, H.R. Kunz, Experimental Methods and Data Analyses for Polymer Electrolyte Fuel Cells, Scribner Associates, Inc., 2005.
[20] R. O'Hayre, W. Colella, S. Cha, F.B. Prinz, Fuel Cell Fundamentals, 2nd edition, Wiley, 2009.
[21] F. Barbir, PEM Fuel Cells: Theory and Practice, Elsevier Academic Press, London, UK, 2005.